Synthetic optical holography with nonlinear-phase reference

Bradley Deutsch,[1] **Martin Schnell,**[2] **Rainer Hillenbrand,**[2,3,5] **and P. Scott Carney**[1,4,*]

[1]*Beckman Institute for Advanced Science and Technology, University of Illinois at Urbana-Champaign, Urbana, IL 61801, USA*
[2]*CIC nanoGUNE and UPV/EHU, 20018 Donostia, San Sebastian, Spain*
[3]*IKERBASQUE, Basque Foundation for Science, 48011 Bilbao, Spain*
[4]*Department of Electrical and Computer Engineering, University of Illinois at Urbana-Champaign, Urbana, Illinois 61801, USA*
[5]*r.hillenbrand@nanogune.eu*
[*]*carney@illinois.edu*

Abstract: Synthetic optical holography (SOH) provides efficient encoding of the complex optical signal, both amplitude and phase, for scanning imaging methods. Prior demonstrations have synthesized reference fields with a plane-wave-like linear variation of the phase with position. To record large images without probe-mirror synchronization, a long-travel, closed-loop reference mirror stage has been required. Here we present SOH with a synthetic reference wave with sinusoidal spatial variation of the phase. This allows the use of open loop, limited mirror travel range in SOH, and leads to a novel holographic inversion algorithm. We validate the theory with scans of graphene grain boundaries from a scanning near-field optical microscope, for which SOH has been shown to drastically increase scan speeds [Nat. Commun. **5**, 3499 (2014)]

© 2014 Optical Society of America

OCIS codes: (090.1995) Digital holography; (170.5810) Scanning microscopy; (180.4243) Near-field microscopy.

References and links

1. D. Gabor, "A new microscopic principle," Nature **161**, 777–778 (1948).
2. P. Hariharan, *Basics of Holography* (Cambridge University, 2002).
3. E. N. Leith and J. Upatnieks, "Reconstructed wavefronts and communication theory," J. Opt. Soc. Am. **52**, 11231130 (1962).
4. J. Rosen and G. Brooker, "Non-scanning motionless fluorescence three-dimensional holographic microscopy," Nat. Photon. **2**, 190–195 (2008).
5. E. Cuche, Y. Emery, and F. Montfort, "Microscopy: One-shot analysis," Nat Photon **3**, 633–635 (2009).
6. G. Nehmetallah and P. P. Banerjee, "Applications of digital and analog holography in three-dimensional imaging," Adv. Opt. Photon. **4**, 472–553 (2012).
7. U. Schnars and W. Jüptner, "Direct recording of holograms by a CCD target and numerical reconstruction," Applied Optics **33**, 179 (1994).
8. U. Schnars and W. Jüptner, *Digital Holography: Digital Hologram Recording, Numerical Reconstruction, and Related Techniques* (Springer, 2004), 2005 ed.
9. T.-C. Poon, *Digital Holography and Three-Dimensional Display: Principles and Applications* (Springer, 2011), softcover reprint of hardcover 1st ed. 2006 ed.
10. C. Mann, L. Yu, C.-M. Lo, and M. Kim, "High-resolution quantitative phase-contrast microscopy by digital holography," Opt. Express **13**, 8693–8698 (2005).

#221476 - $15.00 USD Received 22 Aug 2014; revised 3 Oct 2014; accepted 5 Oct 2014; published 21 Oct 2014
(C) 2014 OSA

11. B. Rappaz, P. Marquet, E. Cuche, Y. Emery, C. Depeursinge, and P. Magistretti, "Measurement of the integral refractive index and dynamic cell morphometry of living cells with digital holographic microscopy," Opt. Express **13**, 9361–9373 (2005).
12. B. Bhaduri, C. Edwards, H. Pham, R. Zhou, T. H. Nguyen, L. L. Goddard, and G. Popescu, "Diffraction phase microscopy: principles and applications in materials and life sciences," Adv. Opt. Photon. **6**, 57–119 (2014).
13. T. Zhang and I. Yamaguchi, "Three-dimensional microscopy with phase-shifting digital holography," Opt. Lett. **23**, 1221–1223 (1998).
14. T.-C. Poon and T. Kim, "Optical image recognition of three-dimensional objects," Appl. Opt. **38**, 370–381 (1999).
15. B. W. Schilling, T.-C. Poon, G. Indebetouw, B. Storrie, K. Shinoda, Y. Suzuki, and M. H. Wu, "Three-dimensional holographic fluorescence microscopy," Opt. Lett. **22**, 1506–1508 (1997).
16. W. S. Haddad, D. Cullen, J. C. Solem, J. W. Longworth, A. McPherson, K. Boyer, and C. K. Rhodes, "Fourier-transform holographic microscope," Appl. Opt. **31**, 4973–4978 (1992).
17. F. Dubois, L. Joannes, and J.-C. Legros, "Improved three-dimensional imaging with a digital holography microscope with a source of partial spatial coherence," Appl. Opt. **38**, 7085 (1999).
18. M. Schnell, P. S. Carney, and R. Hillenbrand, "Synthetic optical holography for rapid nanoimaging," Nat. Commun. **5** (2014).
19. M. Schnell, M. J. Perez-Roldan, P. S. Carney, and R. Hillenbrand, "Quantitative confocal phase imaging by synthetic optical holography," Opt. Express **22**, 15267–15276 (2014).
20. R. P. Porter and A. J. Devaney, "Generalized holography and computational solutions to inverse source problems," J. Opt. Soc. of Am. **72**, 1707 (1982).
21. D. A. Jackson. "Pseudoheterodyne detection scheme for optical interferometers," Elect. Lett. **18**(25), 1081–1083 (1982).
22. N. Ocelic, A. Huber, and R. Hillenbrand, "Pseudoheterodyne detection for background-free near-field spectroscopy," Appl. Phys. Lett. **89**, 101124 (2006).
23. A. Yariv, *Optical Electronics* (Oxford University, 1990).
24. A. Nesci, R. Dändliker, and H. P. Herzig, "Quantitative amplitude and phase measurement by use of a heterodyne scanning near-field optical microscope," Opt. Lett. **26**, 208–210 (2001).
25. Y. Kikuchi, D. Barada, T. Kiire, and T. Yatagai. "Doppler phase-shifting digital holography and its application to surface shape measurement," Opt. Lett. **35**(10), 1548 (2010).
26. D. Barada, T. Kiire, J. Sugisaka, S. Kawata, and T. Yatagai. "Simultaneous two-wavelength Doppler phase-shifting digital holography," Appl. Opt. **50**(34), H237–H244 (2011).
27. T. Kiire, D. Barada, J. Sugisaka, Y.Hayasaki, and T. Yatagai. "Color digital holography using a single monochromatic imaging sensor," Opt. Lett. **37**(15), 3153–3155 (2012).
28. I. Amidror, *Mastering the Discrete Fourier Transform in One, Two or Several Dimensions: Pitfalls and Artifacts* (Springer, 2013).
29. F. Zenhausern, M. P. O'Boyle, and H. K. Wickramasinghe, "Apertureless near-field optical microscope," Appl. Phys. Lett. **65**, 1623–1625 (1994).
30. S. Kawata and Y. Inouye, "Scanning probe optical microscopy using a metallic probe tip," Ultramicrosc. **57**(2-3), 313–317 (1995).
31. R. Bachelot, P. Gleyzes, and A. C. Boccara, "Near-field optical microscopy by local perturbation of a diffraction spot," Microscopy Microanalysis Microstructures **5**(4-6), 389–397 (1994).
32. F. Keilmann and R. Hillenbrand, "Near-field microscopy by elastic light scattering from a tip," Phil. Trans. R. Soc. Lond. A **362**, 787 (2004).
33. R. Esteban, R. Vogelgesang, J. Dorfmüller, A. Dmitriev, C. Rockstuhl, C. Etrich, and K. Kern, "Direct near-field optical imaging of higher order plasmonic resonances," Nano Lett. **8**, 3155–3159 (2008).
34. N. Maghelli, M. Labardi, S. Patan, F. Irrera, and M. Allegrini, "Optical near-field harmonic demodulation in apertureless microscopy," J. Microsc. **202**, 84–93 (2001).
35. T. Taubner, R. Hillenbrand, and F. Keilmann, "Performance of visible and mid-infrared scattering-type near-field optical microscopes," J. Microsc. **210**, 311–314 (2003).
36. R. Hillenbrand and F. Keilmann, "Complex optical constants on a subwavelength scale," Phys. Rev. Lett. **85**, 3029–3032 (2000).
37. Y. Sasaki and H. Sasaki, "Heterodyne detection for the extraction of the probe-scattering signal in scattering-type scanning near-field optical microscope," Japanese J. of Appl. Phys. **39**, 321 (2000).
38. D. Roy, S. H. Leong, and M. E. Welland, "Dielectric contrast imaging using apertureless scanning near-field optical microscopy in the reflection mode," J. Kor. Phys. Soc. **47**, 140 (2005).
39. I. Stefanon, S. Blaize, A. Bruyant, S. Aubert, G. Lerondel, R. Bachelot, and P. Royer, "Heterodyne detection of guided waves using a scattering-type scanning near-field optical microscope," Opt. Expr. **13**, 5553–5564 (2005).
40. A. V. Oppenheim and R. W. Schafer, *Discrete-Time Signal Processing* (Prentice Hall, 2009), 3rd ed.
41. Z. Fei, A. S. Rodin, W. Gannett, S. Dai, W. Regan, M. Wagner, M. K. Liu, A. S. McLeod, G. Dominguez, M. Thiemens, A. H. C. Neto, F. Keilmann, A. Zettl, R. Hillenbrand, M. M. Fogler, and D. N. Basov, "Electronic and plasmonic phenomena at graphene grain boundaries," Nat. Nano. **8**, 821–825 (2013).
42. B. Moslehi, "Noise power spectra of optical two-beam interferometers induced by the laser phase noise," J.

#221476 - $15.00 USD Received 22 Aug 2014; revised 3 Oct 2014; accepted 5 Oct 2014; published 21 Oct 2014
(C) 2014 OSA

Lightwave Tech. **4**, 1704–1710 (1986).
43. Y. Wang, *Optimization and Regularization for Computational Inverse Problems and Applications* (Higher Education, 2011).

1. Introduction

In holography [1–6], an unknown complex signal is encoded as an intensity image such that information is distributed across the whole image through interference with a known reference field. In digital holography, the hologram intensity is recorded on a CCD, and the unknown signal field is retrieved using digital processing [7–9]. This has led in turn to digital holographic microscopy, a wide-field technique providing quantitative phase [10–12]. Such phase information can be used for three-dimensional reconstructions [4, 13–15], numerical refocusing [4, 16, 17], and aberration correction [16]. A recent development in scanning microscopy has extended the holographic concept of distributed phase information to scanning imaging through synthetic optical holography (SOH) [18, 19].

In SOH, the complex field scattered from a focus or a local probe interferes with a reference beam at a one-pixel detector. While the focus or the local probe is scanned across the sample, the amplitude and phase of the reference beam is varied slowly compared to the scanning. Recording the detector signal as a function of position yields a hologram where the complex field is encoded as intensity in a fashion analogous the fringe patterns found in wide-field holograms. The complex field can then be reconstructed by applying a suitable inversion algorithm. The distributed encoding approach offers several advantages in scanning phase imaging applications: fast phase imaging in combination with technical simplicity and simultaneous operation at visible and infrared frequencies. Thus, SOH may become an attractive alternative to interferometric methods of phase imaging which determine the phase at each position of the image independently and so do not take advantage of the mutual information across pixels.

SOH was demonstrated in both scattering-type scanning near-field optical microscopy (s-SNOM) [18] and scanning confocal microscopy [19]. In those cases, a reference field was synthesized with a phase linear in position. Such a reference field may be seen to result in data analogous to those obtained in a holographic measurement with an off-axis plane-wave reference.

Plane waves often have been used as the reference field in holography as they are relatively easy to produce using diffractive optics, and signal retrieval is straight forward. The linear (in position) phase of the plane wave leads to a simple shift of the encoded complex signal in the Fourier domain, and that signal is thus recovered by filtering and shifting in the Fourier domain. However, holography may also be seen as an approximately linear optical inverse problem [20], and so it becomes clear that a large class of reference fields could be used if it were advantageous to do so.

There are practical motives to develop alternatives to a linear-phase reference wave in SOH. SOH uses a translation stage, driven for example by a piezo-electric device, with limited travel range to move the reference mirror. Long-travel-range, closed-loop piezoelectric devices must be used, and the mirror position must be reset occasionally: a process that can lead to errors in positioning or timing. A convenient solution would be to perform the scanning imaging while translating the reference mirror slowly and periodically over a limited range.

Such a movement is potentially easy to perform with a short-range piezo-electric device operated in open loop and would allow to acquire arbitrarily large images without intermittent piezo retraction. Thus, as a specific example, we implement in this paper a reference in which the phase varies sinusoidally rather than linearly with position in the detector plane. This reference field requires a modified inversion algorithm which might be seen to be a multidimensional generalization of pseudoheterodyne interferometry (PHI) [21–24].

#221476 - $15.00 USD Received 22 Aug 2014; revised 3 Oct 2014; accepted 5 Oct 2014; published 21 Oct 2014
(C) 2014 OSA

An analysis different than traditional PHI is required for two reasons. First, the reference phase variation can be mapped to a grid, on which it varies in two spatial dimension rather than one temporal dimension. Second, the spatial variation of the signal manifests as broadband spatial frequency information, whereas the signal is usually taken to be monochromatic (that is sinusoidal) in PHI. The latter difference requires a modified inversion process, and places constraints on the signal and reference fields.

In Section 2, Fourier holography and SOH are briefly reviewed. In Section 3 we model data collection, and present an algorithm for retrieving the amplitude and phase. In Section 4 the approach is validated in a s-SNOM experiment, and noise considerations are discussed.

2. Synthetic optical holography

SOH was recently developed as a way to bring the advantages of digital holography [18, 19] to scanning imaging methods. Figure 1 is a sketch of the basic SOH setup. We wish to determine the complex value of a field $U_S(\mathbf{r})$ with full spatial bandwidth Δk_S located in a plane z_S, typically generated by a sample. A point detector is placed in the image plane, and the sample is scanned to collect a grid of equally spaced intensity values. At the detector, the signal interferes with a time-varying reference field $U_R(t)$, whose phase is dictated by the displacement of a reference mirror along the z axis. The result is a two-dimensional grid of intensity values denoted by I_{ab} at each pixel index (a,b).

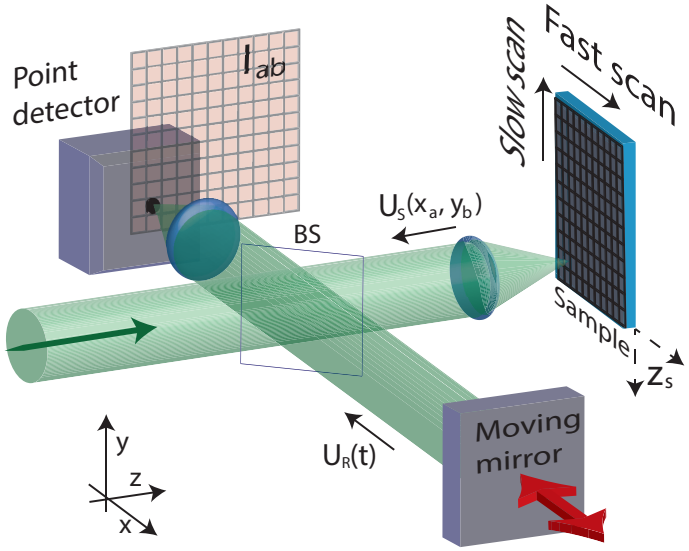

Fig. 1. Sketch of setup for synthetic optical holography. The sample is scanned while the reference mirror moves, creating a time-dependent reference phase. A point detector is used to assemble a holographic intensity map.

The sampled signal field at each pixel is simply

$$U_{S,a,b} = U_S(x_a\hat{x} + y_b\hat{y}). \tag{1}$$

Once a particular scan pattern is chosen, the reference field can be reparameterized by pixel index rather than time. As long as the reference phase varies slowly with respect to the integration time, the sampled reference field at pixel (a,b) is given by $U_{R,a,b} = U_R(x_a\hat{x} + y_b\hat{y})$ (where

#221476 - $15.00 USD Received 22 Aug 2014; revised 3 Oct 2014; accepted 5 Oct 2014; published 21 Oct 2014
(C) 2014 OSA

the time dependence at optical frequencies has been suppressed). The recorded intensity value at this pixel is

$$I_{a,b} = |U_{S,a,b} + U_{R,a,b}|^2 = |U_{S,a,b}|^2 + |U_{R,a,b}|^2 + U^*_{S,a,b}U_{R,a,b} + U_{S,a,b}U^*_{R,a,b} \tag{2}$$

The basic task of digital holography is to use an inversion algorithm to extract a quantity proportional to $U_{S,a,b}$ from the data $\sum_{a,b} I_{a,b}$. The specific inversion algorithm depends on which reference field, $U_R(t)$, is chosen and what is known *a priori* about the unknown field.

For the remainder of the manuscript, we will assume that the scanning is in on a rectangular Cartesian grid with uniform sampling so that $x(t) = v_x t$ and $y(t) = v_y t$ and measurements are made at times $t_{a,b}$ to correspond with points $\mathbf{r}_{a,b} = (x_a, y_b)$ on the sampling grid $x_a = a\Delta_x + x_0$, $y_b = b\Delta_y + y_0$. If the mirror in the reference arm is moved also in a fashion linear in time, that is the reference arm introduces an additional path length d such that $d = 2v_R t$, then $U_{R,a,b} = A_R e^{i\left(k_x x_a + k_y y_b\right)} = A_R e^{i\mathbf{k}_\parallel \cdot \mathbf{r}_{a,b}}$. The effective wavevector, $\mathbf{k}_\parallel$, is given by $k_x = 4\pi v_R/(v_x\lambda)$ and $k_y = 4\pi v_R/(v_y\lambda)$ where λ is the wavelength of the light. Assume $\mathbf{k}_\parallel$ lies on the reciprocal lattice of the sampling grid, explicitly $k_x = \ell_x 2\pi/[(N_x-1)\Delta_x]$, and $k_y = \ell_y 2\pi/[(N_y-1)\Delta_y]$,where N_j is the number of sample points in direction j and ℓ_x and ℓ_y are integers. In the discrete Fourier transform (DFT) domain the recorded intensity is given by the expression

$$\tilde{I}_{p,q} = |A_R|^2\delta_{p,q} + \tilde{C}_{p,q} + A_R\tilde{U}^*_{S,\ell_x-p,\ell_y-q} + A^*_R\tilde{U}_{S,\ell_x+p,\ell_y+q}, \tag{3}$$

where a tilde indicates a DFT, $\delta_{p,q}$ is the Kronicker delta function , and $\tilde{C}_{p,q} = DFT\left[|U_{S,a,b}|^2\right]$ is the DFT of the *autocorrelation* term. The final two terms are copies of the unknown field, offset from the origin and referred to as the conjugate and direct terms, respectively. This situation is very much like that seen in Leith-Upatnieks off axis holography. A simulation is shown in Fig. 2 to demonstrate the linear phase, the resulting fringe pattern in the hologram, and the separation of the direct and conjugate terms.

The unknown field may be recovered from Eq. (3) in a straight forward manner if the field is sufficiently band-limited and $\mathbf{k}_\parallel$ is sufficiently large. For sufficiently large values of A_R, it can be assumed that $\tilde{C}_{p,q}$ is negligible. The DFT of the intensity, filtered with a window centered at $(-\ell_x, -\ell_y)$ (the width of which is set to a maximum of $\ell_x/2, \ell_y/2$ in each dimension) and shifted to the origin, yields $\tilde{U}_S$, the DFT of the unknown signal. This is demonstrated in Fig. 2 where the two grey-scale images are encoded as the real and imaginary parts of the field. Each image is 2048×2048 pixels. The wavevector $\mathbf{k}_\parallel$ is chosen so that the phase of the reference cycles through 2π every 4 pixels in the horizontal, or x, direction, and every 10 pixels in the vertical, or y, direction. The complex image is recovered from the data indicated in the red box in panel (e) and the resultant real and imaginary parts are shown in panels (f) and (g).

When $\tilde{C}_{p,q}$ is not negligible, $\mathbf{k}_\parallel$ must be larger or the filter narrower, or both. If $\mathbf{k}_\parallel$ is not on the reciprocal lattice, then $\mathbf{k}_\parallel = (\ell_x 2\pi/[(N_x-1)\Delta_x], \ell_y 2\pi/[(N_y-1)\Delta_y]) + \Delta\mathbf{k}$ and the procedure described above needs to be augmented with a subpixel shift in the Fourier domain, or, equivalently, by multiplying the results by $e^{i\Delta\mathbf{k}\cdot\mathbf{r}}$. Among many advantages of the linear-phase approach is that a great deal of work has been done to develop the necessary tools of signal analysis to recover U_S [7–9].

3. Sinusoidal-phase reference wave

In principle, the phase of reference field U_R can be chosen as any function of position by controlling the position of the reference mirror in time. The methods used in SOH with linear-phase reference waves offer the advantage of drawing on well-established techniques in signal processing. However, to create the linear-phase synthetic reference wave, the mirror in the reference arm must have a long travel range. For instance, with $\lambda = 10\mu$m, a square megapixel

#221476 - $15.00 USD Received 22 Aug 2014; revised 3 Oct 2014; accepted 5 Oct 2014; published 21 Oct 2014
(C) 2014 OSA

image requires travel of the reference arm mirror of more than 1.25 mm. To avoid this requirement and gain other advantages discussed below, we set the reference mirror to oscillate about its zero position sinusoidally, creating a reference of the form

$$U_R(t) = A_R e^{i\gamma \sin(2\pi f t + \phi)}, \tag{4}$$

where γ is the modulation amplitude in radians, f is the oscillation frequency in Hz, and ϕ is a phase offset generated when the mirror zero position does not coincide with the scan zero position.

There is precedent for the choice of a sinusoidal-phase reference wave. The resulting interference pattern is the basis for pseudoheterodyne interferometry, which was invented more than thirty years ago [21]. More recently, sinusoidal mirror motion has been used in wide-field digital holography [25–27]. In contrast to previous work, here phase information about the object is shared among pixels and collected as a spatially varying intensity, and we will see that the non-zero spatial bandwidth of the object results in special concerns in the demodulation step typical to such techniques.

The sampled sinusoidal-phase reference is

$$U_{R,a,b} = A_R \exp\left[i\gamma \sin\left(2\pi\left(\left(f - N f_{s,x}\right) x_a / v_x + \left(f - M f_{s,y}\right) y_b / v_y\right) + \phi\right)\right], \tag{5}$$

where $f_{s,x}$ and $f_{s,y}$ are the sampling frequencies in the fast and slow scan directions respectively, v_x and v_y are the scan velocities, and N and M are integers which account for the possibility of aliasing [28]. The sampling frequencies are discussed further in section 3.2.

We define a wavevector for the sinusoidal case, $\mathbf{k}_\parallel$, with $k_x = 2\pi\left(f - N f_{s,x}\right)/v_x$ and $k_y = 2\pi\left(f - N f_{s,y}\right)/v_y$. The reference field may be expressed in terms of plane-wave components by the Jacobi-Anger expansion,

$$U_{R,a,b} = A_R e^{i\gamma \sin\left(\mathbf{k}_\parallel \cdot \mathbf{r} + \phi\right)} = A_R \sum_{n=-\infty}^{\infty} J_n(\gamma)\, e^{in\left(\mathbf{k}_\parallel \cdot \mathbf{r} + \phi\right)}. \tag{6}$$

The intensity from Eq. (2) thus becomes

$$I_{a,b} = |U_{S,a,b}|^2 + |A_R|^2 + A_R U^*_{S,a,b} \sum_{n=-\infty}^{\infty} J_n(\gamma)\, e^{in\phi} e^{in\mathbf{k}_\parallel \cdot \mathbf{r}_{a,b}} + c.c. \tag{7}$$

Taking a DFT, we have

$$\begin{aligned} \tilde{I}_{p,q} = {} & |U_{S,a,b}|^2 \delta_{p,q} + \tilde{C}_{p,q} + A_R \sum_{n=-\infty}^{\infty} J_n(\gamma)\, e^{in\phi} \tilde{U}^*_{S,n\ell_x - p, n\ell_y - q} \\ & + A_R^* \sum_{n'=-\infty}^{\infty} J_{n'}(\gamma)\, e^{-in'\phi} \tilde{U}_{S,n'\ell_x + p, n'\ell_y + q}. \end{aligned} \tag{8}$$

It is convenient to replace $n' \to -n$ in the second summation and apply the Bessel function identity $J_{-m}(x) = (-1)^m J_m(x)$, allowing us to combine the two summations with the result

$$\tilde{I}_{p,q} = |U_{R,a,b}|^2 \delta_{p,q} + \tilde{C}_{p,q} + \sum_{n=-\infty}^{\infty} J_n(\gamma)\, e^{in\phi} \left(A_R \tilde{U}^*_{S,n\ell_x - p, n\ell_y - q} + (-1)^n A_R^* \tilde{U}_{S,p - n\ell_x, q - n\ell_y}\right). \tag{9}$$

This is the discrete Fourier transform of the intensity as a function of position, analogous to Eq. (3). There are several points in this result that deserve comment. First, as in the linear case, the autocorrelation may be neglected or filtered, and the constant background manifesting as

#221476 - $15.00 USD Received 22 Aug 2014; revised 3 Oct 2014; accepted 5 Oct 2014; published 21 Oct 2014
(C) 2014 OSA

the first term in Eq. (9) may also be eliminated by filtering. Second, the terms appearing in the parentheses under the summation are grouped so that, for each value of n, the d.c. part (the zero spatial frequency) is shifted from the origin by $n\cdot(\ell_x,\ell_y)$. Third, for each value of n the quantity in the parentheses may be seen to be proportional to the Fourier transform of the real or imaginary parts of the field depending on whether n is even or odd respectively. That is $2\widetilde{\mathrm{Re}U}(\mathbf{q})=\tilde{U}^*(-\mathbf{q})+\tilde{U}(\mathbf{q})$ and $2i\widetilde{\mathrm{Im}U}(\mathbf{q})=\tilde{U}(\mathbf{q})-\tilde{U}^*(-\mathbf{q})$. Fourth, the wavevector, $\mathbf{k}_\parallel$, or the corresponding integer pixel index version (ℓ_x,ℓ_y), is completely independent of the wavelength of the light, and instead determined by the velocities of the mirror, the scanning probe and the sampling rate. This stands in contrast to the linear case, in which the wavevector is inversely proportional to the wavelength. Fifth, the infinite series of copies of the real and imaginary parts of the field falls off rapidly and so may safely be truncated at some point. However, as may be seen in Fig. 2, it is certainly possible to put nonnegligible amounts of energy into high-order terms which will alias, or wrap around in the Fourier domain. The weighting given to each term is determined by the modulation depth which is where the wavelength affects the hologram. A shift in wavelength results in a change in weightings among the terms. This too stands in contrast to the linear case where a shift in wavelength results in a shift in the Fourier space.

3.1. Inversion

In order to retrieve U_S, we must combine at least two of the terms from the summation in Eq. (9) with indices $n=2m-1$ (odd) and $n=2m$ (even), $m\in\mathbb{Z},\neq 0$. Each term is then filtered with a window centered at $(n\ell_x,n\ell_y)$ and shifted to the origin by $(-n\ell_x,-n\ell_y)$, the result written $\tilde{I}_n$. The odd terms, after filtering and shifting, are

$$\tilde{I}_{2m-1,p,q}=J_{2m-1}(\gamma)\,e^{i(2m-1)\phi}\left(A_R\tilde{U}^*_{S,-p,-q}-A^*_R\tilde{U}_{S,p,q}\right),$$

and the even terms are

$$\tilde{I}_{2m}=A_RJ_{2m}(\gamma)\,e^{i(2m)\phi}\left(A_R\tilde{U}^*_{S,-p,-q}+A^*_R\tilde{U}_{S,p,q}\right).$$

Taking an inverse DFT of these values and rearranging yields the real and imaginary parts of the unknown field. We can define two terms

$$Y=\frac{I_{2m-1}}{2J_{2m-1}(\gamma)\exp(i\hat{\phi}_{2m-1})}=\mathrm{Im}\{A^*_RU_S\},\tag{10}$$

and

$$X=\frac{I_{2m}}{2J_{2m}(\gamma)\exp(i\hat{\phi}_{2m})}=\mathrm{Re}\{A^*_RU_S\}.\tag{11}$$

where $\hat{\phi}_n$ is the phase of I_n. The unknown field is then simply

$$U_S=\frac{A_R(X+iY)}{|A_R|^2}.\tag{12}$$

Both X and Y theoretically lie along radial lines in the complex plane, and $\hat{\phi}_n$ should therefore be identical at every pixel in I_n. In practice, small variations cause the phase to differ slightly at each pixel in I_n, and some kind of estimation must be used. In this manuscript, the phase is rounded to the nearest 0.01 radians, and the mode is chosen as a measure of $\hat{\phi}_n$.

As in the linear case, if $\mathbf{k}_\parallel$ does not lie on the reciprocal lattice of the spatial sampling grid, a linear phase ramp will appear in the reconstruction. This may be eliminated by several approaches, including simply multiplication by the appropriate compensating phase ramp. Making small adjustments to k_x and k_y until I_1 has a flat phase eliminates the need to know these values *a priori*.

#221476 - $15.00 USD Received 22 Aug 2014; revised 3 Oct 2014; accepted 5 Oct 2014; published 21 Oct 2014
(C) 2014 OSA

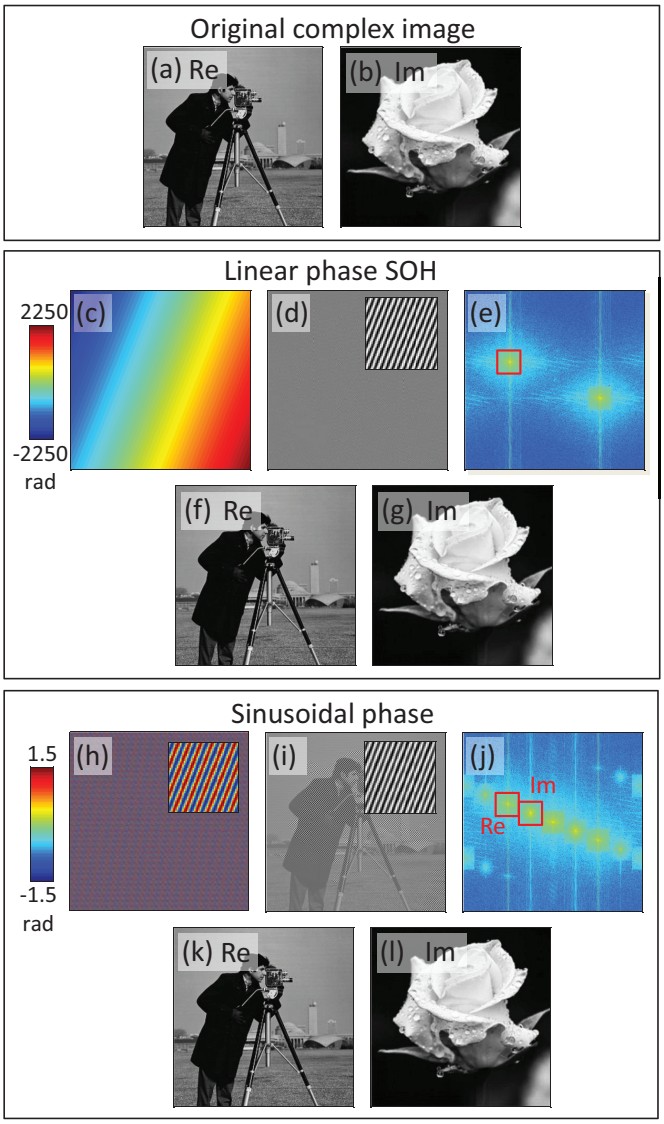

Fig. 2. Simulations of SOH with linear- and sinusoidal-phase reference waves. The real and imaginary part of the original complex-valued image are shown in panels (a) and (b) respectively. The mirror position in radians as a function of position in the scanned image is shown in (c) and the resulting hologram is shown in (d) with a 41× zoom inset. The Fourier transform of the hologram is shown in (e) demonstrating the separation of the direct and conjugate images with the filter used indicated by the red box. The recovered images are shown in panels (f) and (g). The mirror position for sinusoidal-phase SOH is shown in panel (h) with resulting hologram and 41× zoom showing the fringe pattern in (i). The Fourier transform of the hologram is shown in (j) with the two filters used to recover the real and imaginary parts of the field indicated by red boxes. The recovered images are shown in (k) and (l).

#221476 - $15.00 USD Received 22 Aug 2014; revised 3 Oct 2014; accepted 5 Oct 2014; published 21 Oct 2014
(C) 2014 OSA

It is also necessary to take care to set the mirror modulation depth such that none of the denominators $J_{2m-1}(\gamma)$ nor $J_{2m}(\gamma)$ is close to 0 for any of the terms used in the reconstruction as this clearly yields an unstable solution. Choosing a small modulation depth along with small m enforces this constraint.

The sinusoidal phase variation is demonstrated in the simulation in Fig. 2. The resultant hologram and fringes are shown. The same images were used as in the linear case. The wavevectors were set so that the mechanical mirror phase, that is $\mathbf{k}_{\|} \cdot \mathbf{r}$, cycles through 2π every 8 pixels in the horizontal direction and every 20 pixels in the vertical direction. The mirror oscillation depth is set to 1.5 radians (3 radians peak-to-peak).

The Fourier transform is shown in panel (j) where multiple orders may be seen. The $n = 1$ and $n = 2$ orders have been highlighted in red boxes and labeled *Re* and *Im*, and encode the quantities X and Y given in Eqs. (10) and (11). The real and imaginary parts of the reconstruction are obtained by filtering and shifting the data in the red boxes in accordance with Eqs. (10), (11), and (12).

3.2. Wavevector and scan parameters

The raster-scan pattern is specified by the forward scan speed in pixels per second (v_f), the backward scan speed (v_b), the wait time per slow scan line (T_w) in which the sample is not scanning, the number of pixels in the fast-scan direction (n_x), and the time between pixels in the fast scan direction (t_x). The sampling frequency in the fast direction is $f_x = 1/t_x$. For a mirror oscillation frequency f in Hz, the spatial frequency of the phase sinusoid in the fast-scan direction is $k_y = 2\pi(f - Mf_{s,x})/v_x$ in oscillations per pixel. The mirror frequency f can be easily chosen small enough that $M = 0$. The spatial frequency in the slow-scan direction is

$$k_y = 2\pi(f - Mf_{s,y})/v_y = 2\pi(f - Mf_{s,y})\left(\frac{n_x}{v_f} + \frac{n_x}{v_b} + T_w\right). \tag{13}$$

Care must be taken to ensure that each filtered Fourier term contains only negligible contributions from neighboring terms. To that end, the spacing between terms must be larger than the spatial bandwidth of the sampled object. Practically, the filter applied to each Fourier term in Eq. (9) should capture the full bandwidth of U_S while not overlapping with other terms. In general, this imposes two constraints. First, k_x and k_y should be chosen such that $\Delta k_{S,j} < k_j$ for $j \in (x,y)$. This ensures that the full bandwidth of the signal can be captured without interference from neighboring terms. Second, care must be taken to avoid interference from high-spatial-frequency terms since they wrap around the Fourier plane. There are two ways to do this: the modulation depth of the mirror can be kept small so that $J_n(\gamma)$ is negligible for $n > \mathrm{ArgMin}\{n_x/2l_x, n_y/2l_y\}$, or k_x can be chosen large enough that the wrapped Fourier terms are safely shifted to in the horizontal direction and do not interfere with the non-wrapped terms, i.e. $k_x > \Delta k_{S,x} k_x/n_x$. The former strategy was employed in the experimental data presented here. The object can be oversampled in one or both dimensions to ensure that these constraints are met. In some experiments, it may be cumbersome to control T_w, or to make v_y different from v_b. In that case, the Fourier terms can be arranged by making small changes to the mirror oscillation frequency.

4. Experimental validation

We demonstrate SOH with a sinusoidal-phase reference wave by s-SNOM imaging the same graphene grain boundary as in [18]. s-SNOM [29–32] is a scanning microscopy technique that circumvents the diffraction limit and provides nanoscale spatial resolution at visible, infrared and THz wavelengths by recording the light scattered at a scanning probe tip. Detection of both

#221476 - $15.00 USD Received 22 Aug 2014; revised 3 Oct 2014; accepted 5 Oct 2014; published 21 Oct 2014
(C) 2014 OSA

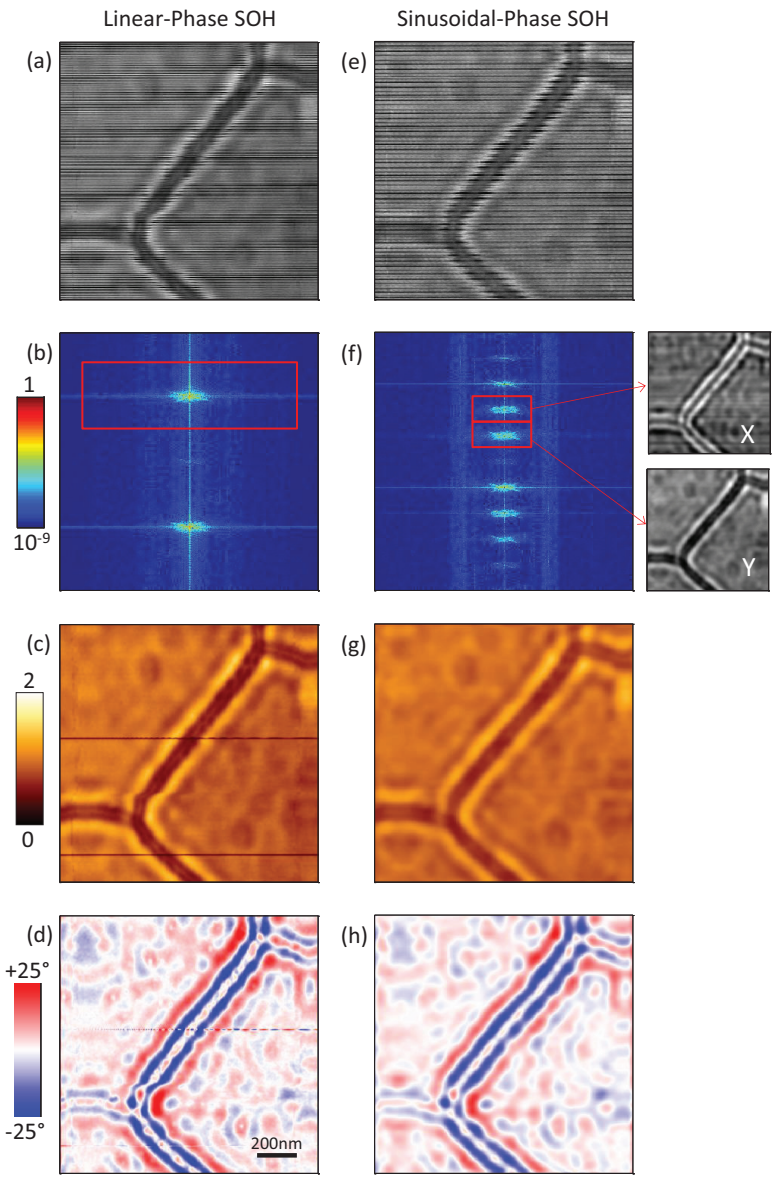

Fig. 3. Experimental results for both linear- and sinusoidal-phase reference waves. The hologram for the linear case is shown in panel (a) with logarithm of the absolute values of the Fourier transform in panel (b). The magnitude and phase of the linear case reconstructions are shown in panels (c) and (d). The hologram for the sinusoidal case is shown in panel (e) with logarithm of the absolute values of the Fourier transform in panel (f). The inverse Fourier transforms of the data shown in the red boxes, corresponding to *X* and *Y* are shown in the call-outs. The resultant magnitude and phase of the sinusoidal case reconstructions are shown in panels (g) and (h).

#221476 - $15.00 USD Received 22 Aug 2014; revised 3 Oct 2014; accepted 5 Oct 2014; published 21 Oct 2014
(C) 2014 OSA

the amplitude and phase of the tip-scattered light is desirable because it provides the full suppression of background contributions and enables access to the near-field phase [22]. To this end, different interferometric detection methods have been implemented in s-SNOM such as quadrature homodyne [33–35], heterodyne [36–39] and pseudoheterodyne [22] detection. With the recent introduction of SOH, a fast and technically easy alternative to these interferometic methods was presented [18]. In s-SNOM, SOH enables rapid nanoimaging, e.g. the acquisition of megapixel near-field images on the time scale of ten minutes, and imaging at two (and potentially even more) wavelengths simultaneously. While only linear-phase reference waves have been considered so far, in the following we will implement and demonstrate SOH with sinusoidal-phase reference waves in s-SNOM.

Our s-SNOM is based on an atomic force microscope where a sharp metal probe is brought into near-contact with a sample. When the tip is illuminated with a monochromatic focused laser beam, it scatters the local near field into propagating modes which becomes the signal field U_S above. The tip-scattered field U_S is collected by a parabolic mirror and interfered at the detector with a sinusoidal-phase reference field U_R. The latter is generated by reflection from a piezo-actuated mirror that is slowly moved in a sinusoidal fashion. To suppress background contributions in U_S, the probe is made to oscillate vertically at a frequency Ω and the detector signal is demodulated at a higher-harmonic frequency $n\Omega$ [34]. Specifically, while the sample is scanned, the demodulated detector signal is recorded at the $n = 3$ harmonic as a function of position and a near-field hologram is obtained. For comparison, we also performed SOH with a linear-phase reference wave with the same setup and under the same conditions as has been described in [18]. In this case, the piezo-actuated mirror is slowly moved at constant velocity.

The results for the sinusoidal and linear cases of SOH SNOM are shown in Fig. 3. In the sinusoidal case (right column), the measurement was accomplished with a significantly shorter translation of the reference mirror, $3.74\mu m$ as compared to $1360\mu m$ in the linear case (left column), and the piezo was operated in open loop, simplifying acquisition (Physikinstrumente, model P-611). The illumination wavelength was $10.6\mu m$, and the line rate for cases was 4.95 lines per second. The reference mirror modulation depth was measured with the position sensors in the piezo stage to be $3.74\mu m$ (peak-to-peak), corresponding to $\gamma = 2.22$ radians, and its oscillation frequency was set such that it one oscillation was completed in ten scan lines. Thus, $M = N = 0$ in Eqs. (5) and (13). Note that in the linear case, the large travel range of $1360\mu m$ required two intermittent piezo retracts during image acquisition because the range of the employed piezo stage was limited to $600\mu m$ (Physikinstrumente, model PiHera PI-628). These retracts produced two horizontal stripes in the images in Figs. 3(c) and 3(d). Such piezo retractions are entirely avoided in the sinusoidal case, allowing for the acquisition of arbitrarily large images without artifacts.

The scan parameters used to acquire the data shown in Fig. 3 resulted in the Fourier terms from Eq. (9) being arranged nearly vertically, with power being distributed mostly among the first three terms. Note that by choosing different scan parameters, the arrangement and energy distribution can be modified. The near-field hologram in Fig. 3(e) shows a fast variation in the slow scan (vertical) direction. The Fourier terms at multiples of $\mathbf{k}_{\|}$ are present along a nearly vertical line in the Fourier transform. As shown above, we require one even term and one odd term to reconstruct the object. In this example, we take the $n = +1$ and $+2$ terms, which are filtered using a Hanning window [40] and shifted to DC. The image was oversampled by a factor of four in the slow-scan direction to ensure enough separation between Fourier terms resulting in a hologram that is 256×1024 pixels. The window width was set to $\sim 0.23 n_x$. The real and imaginary parts of the image are constructed from the $n = +2$ and $n = +1$ terms separately (shown in the call outs). The amplitude and phase were calculated then from Eq. (12) and displayed in panels (g) and (h) of Fig. 3. The images show interference fringes resulting

#221476 - $15.00 USD Received 22 Aug 2014; revised 3 Oct 2014; accepted 5 Oct 2014; published 21 Oct 2014
(C) 2014 OSA

from the reflection of plasmons from the graphene grain boundaries [18, 41].

We note that since the filters used in the sinusoidal-phase case are smaller than those in the linear phase, the retrieved objects appear to have smoother edges. Indeed, there is a tradeoff between the simplicity of the equipment (open loop, short-range piezos) and the object bandwith for the same size data set. However, if sharper edges are required, the object may be sampled on a finer grid in order to keep the filter size similar to that used in the linear case. This is accomplished at the cost of scan speed for a given SNR.

About 5% of the image was cropped on all sides because of scan stage instabilities during stop/start and turnaround. These reconstructed images are similar to the results obtained with pseudoheterodyne interferometry in [41].

The higher-order terms appearing in the Fourier domain may, in principle, be use to reconstruct the complex field. We demonstrate this in Fig. 4. The second and third order terms are used to calculate the real and imaginary parts of the susceptibility, respectively, as indicated by the red boxes in the Fourier domain image. The use of the higher-order terms may provide some advantage in reducing certain types of additive noise, which we discuss below.

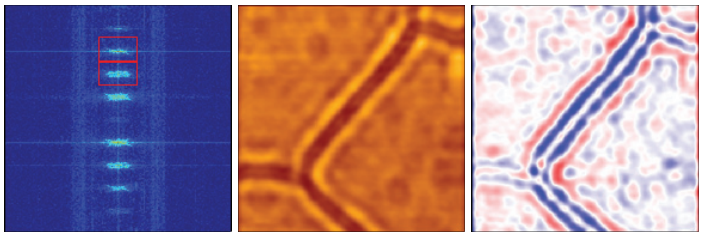

Fig. 4. Reconstructions computed from the second and third order terms of the sinusoidal-phase hologram as indicated by the red boxes in the Fourier domain image (left), resulting in the amplitude (center) and phase (right) images shown.

4.1. Noise considerations

It may be advantageous to include additional Fourier terms from Eq. (9) to improve SNR depending on the noise in the system. For example, we might assume the presence of phase drift in the interferometer, resulting in noise that is multiplicative in the intensity, or shot noise, which is additive. In the case that both are present, the intensity is given by

$$I_{a,b} = I_{0,a,b}(1+\varepsilon_{1,a,b}) + \varepsilon_{2,a,b}, \tag{14}$$

where I_0 is the noiseless intensity, ε_1 represents multiplicative noise, and ε_2 represents additive noise. The subscripts (a,b) have been included to remind us of the domain of the intensity.

Taking a DFT gives

$$\tilde{I}_{p,q} = \tilde{I}_{0,p,q} + \tilde{I}_{0,p,q} * \tilde{\varepsilon}_{1,p,q} + \tilde{\varepsilon},_{2,p,q}\,. \tag{15}$$

where $*$ represents a convolution.

The spatial power spectrum of ε_2 can be considered uniform if it comes from shot noise. The multiplicative noise results from randomness in the optical path difference, and its power spectrum would be expected to fall off at high spatial frequencies [42]. The convolution in Eq. (15) means that identical copies of the multiplicative noise are reproduced at every Fourier term, so the inclusion of additional terms does not help mitigate it. However, if the intensity is dominated by additive noise, it may be useful to include additional Fourier terms.

#221476 - $15.00 USD Received 22 Aug 2014; revised 3 Oct 2014; accepted 5 Oct 2014; published 21 Oct 2014
(C) 2014 OSA

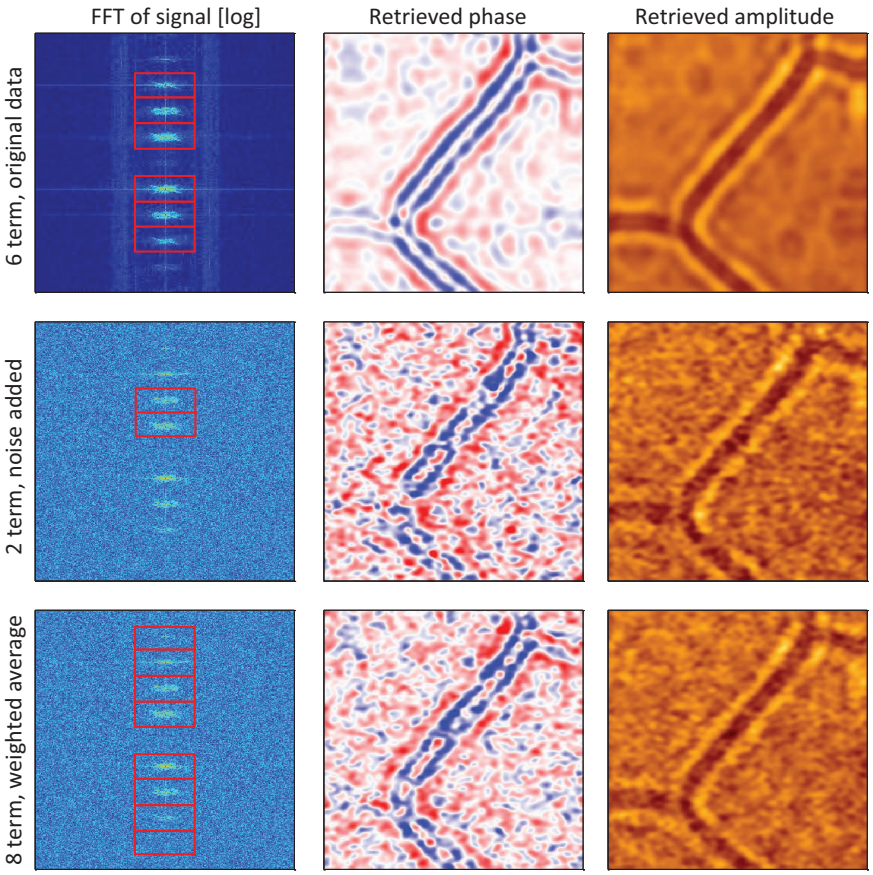

Fig. 5. Example of multiple-term reconstruction with simulated noise. Top row: Original data with 6-term reconstruction. Middle row: Two-term reconstructed with simulated Gaussian white noise added to interferogram in the spatial domain. The noise is mostly evident in the phase reconstruction. Bottom row: Eight term reconstruction with simulated noise and $\alpha = 1$. The result is improved over the two-term case.

#221476 - $15.00 USD Received 22 Aug 2014; revised 3 Oct 2014; accepted 5 Oct 2014; published 21 Oct 2014
(C) 2014 OSA

The general procedure for doing so is as follows. Define a set of odd indices $\mathscr{M}, |\mathscr{M}| = M$, and a set of even indices $\mathscr{N}, |\mathscr{N}| = N$. For each index, the DFT of the intensity is filtered, shifted, and an inverse DFT is taken as in the two-term case above. The retrieved complex signal U_S is given by

$$U_S = X'_\alpha + iY'_\alpha \tag{16}$$

where X' and Y' are, for a weighting parameter $\alpha \in [0,1]$, sums over the even and odd terms, i.e.

$$Y'_\alpha = \frac{1}{2}\sum_{m\in\mathscr{M}} \frac{I_m}{J_m(\gamma)\,exp\left[i\hat{\phi}_m\right]} \frac{\alpha|J_m(\gamma)|+1-\alpha}{\sum_{m'}(\alpha|J_{m'}(\gamma)|+1-\alpha)} \tag{17}$$

and

$$X'_\alpha = \frac{1}{2}\sum_{n\in\mathscr{N}} \frac{I_n}{J_n(\gamma)\,exp\left[i\hat{\phi}_n\right]} \frac{\alpha|J_n(\gamma)|+1-\alpha}{\sum_{n'}(\alpha|J_{n'}(\gamma)|+1-\alpha)}. \tag{18}$$

Note that as $\alpha \to 0$, these equations indicate a straight average over the Fourier terms as indicated by Eqs. (10) and (11), and as $\alpha \to 1$, they indicate a weighted average proportional to each term's magnitude (i.e. its SNR for additive white noise), which is advantageous for noisy data. As in the two-term case, care must be taken that the Bessel functions are not close to zero, or the solution is unstable. Further regularization could be used to improve the stability [43].

Figure 5 is an illustration of the above procedure. The first row shows the original data inverted using the $j = \pm(1,2,3)$ terms. Since we have a high SNR, we see little to no improvement over the two-term inversion in Fig. 3. In the subsequent rows, we have computationally added Gaussian-distributed additive white noise to the recorded intensity signal (the SNR was set to ~ 1.2). The middle row shows the result of the two-term inversion, which includes a strong complex error, particularly visible in the phase. The bottom row shows the result of applying Eqs. (17) and (17) to eight Fourier terms with α set to 1, implying an average with weights equal to $|J_m|$. The result of including eight terms in this case is a clear improvement over the two-term case, with the grain boundaries being more visible and better defined.

5. Conclusion

We have introduced a new option in SOH which uses a sinusoidal-phase reference wave to perform synthetic digital optical holography. We have provided guidelines for experimental design and an algorithm for inversion of the data, and we have discussed scan parameters and noise concerns. Synthetic optical holography provides the means to construct sinusoidal-phase references, which solve challenges in SOH eliminating mirror travel range as a limiting factor. Comparing SOH-based and pseudoheterodyne-based s-SNOM it should be noted that in the latter, the mirror frequency must be on the order of the pixel rate, whereas sinusoidal-phase SOH requires only that the mirror oscillation frequency is on the order of the line rate, dramatically increasing the imaging speed. Sinusoidal-phase reference waves are also an example of a broader class of reference waves not normally seen in digital holography which are now easily accessible with SOH.

Acknowledgments

This work was financially supported by the ERC Starting Grant No. 258461 (TERATOMO) and in part by the Beckman Fellows program.

#221476 - $15.00 USD Received 22 Aug 2014; revised 3 Oct 2014; accepted 5 Oct 2014; published 21 Oct 2014
(C) 2014 OSA